Fall 2014

Transport in Ultra-Thin Heat Pipes for Low Power Applications

Yashwanth Yadavalli

Recommended Citation

Yadavalli, Yashwanth, "Transport in Ultra-Thin Heat Pipes for Low Power Applications" (2014). *Open Access Theses*. 398.
https://docs.lib.purdue.edu/open_access_theses/398

Graduate School Form 30
(Revised 08/14)

PURDUE UNIVERSITY
GRADUATE SCHOOL
Thesis/Dissertation Acceptance

This is to certify that the thesis/dissertation prepared

By Yashwanth Yadavalli

Entitled
Transport in Ultra-Thin Heat Pipes for Low Power Applications

For the degree of Master of Science in Mechanical Engineering

Is approved by the final examining committee:

Prof. Suresh V. Garimella

Dr. Justin A. Weibel

Dr. Xiulin Ruan

Prof. Michael T. Harris

To the best of my knowledge and as understood by the student in the Thesis/Dissertation Agreement, Publication Delay, and Certification/Disclaimer (Graduate School Form 32), this thesis/dissertation adheres to the provisions of Purdue University's "Policy on Integrity in Research" and the use of copyrighted material.

Approved by Major Professor(s): Prof. Suresh V. Garimella

Dr. Justin A. Weibel

Approved by: Prof. Ganesh Subbarayan 10/07/2014

Head of the Department Graduate Program Date

TRANSPORT IN ULTRA-THIN HEAT PIPES FOR LOW POWER APPLICATIONS

A Thesis

Submitted to the Faculty

of

Purdue University

by

Yashwanth Yadavalli

In Partial Fulfillment of the

Requirements for the Degree

of

Master of Science in Mechanical Engineering

December 2014

Purdue University

West Lafayette, Indiana

TABLE OF CONTENTS

APPENDICES

LIST OF TABLES

LIST OF FIGURES

Figure Page

Appendix Figure

NOMENCLATURE

A	area, m^2
C	specific heat capacity, J/kg K
h_{fg}	latent heat, J/kg
k	thermal conductivity, W/m K
K	permeability, m^2
L	length, m
m	mass flow rate, kg/s
$m^{''}$	mass flux, kg/m^2 s
M	figure of merit $[(\rho_l \sigma_l L)/\mu_l]$
M_v	vapor figure of merit $[(h_{fg}^2 \rho_v P_v)/(\mathrm{R}\,\mu_v T_v^2)]$
q''	heat flux, W/m^2
P	pressure, Pa
P_{cap}	capillary pressure, Pa
P_v	saturated vapor pressure, Pa
R	thermal resistance, K/W
R	gas constant, J/kg K
r	thickness ratio
t	thickness, m
t_{limit}	limiting thickness, m
T	temperature, K
u	x-direction velocity, m/s
v	y-direction velocity, m/s

x	axial coordinate, m
y	transverse coordinate, m

Greek symbols

ρ	density, kg/m^3
φ	porosity
μ	dynamic viscosity, N/m
σ	surface tension, Ns/m^2
$\hat{\sigma}$	accommodation coefficient

Subscripts

0	reference
a	adiabatic
c	condenser
e	evaporator
eff	effective
ext	external
i	interface
v	vapor
l	liquid
s	solid
wl	wall
w	wick
HP	heat pipe
HS	heat spreader

ABSTRACT

Yadavalli, Yashwanth. M.S.M.E., Purdue University, December 2014. Transport in Ultra-Thin Heat Pipes for Low Power Applications. Major Professors: Dr. Suresh V. Garimella and Dr. Justin A. Weibel, School of Mechanical Engineering.

Heat pipes and vapor chamber heat spreaders offer a potential solution to the increasing thermal management challenges in thin-form-factor mobile computing platforms, where efficient spreading is required to simultaneously prevent overheating of internal components and formation of hot regions on the device exterior surfaces. The operating conditions for such applications are also characterized by low input heat fluxes, which in combination with the geometric constraints, give rise to unique performance limitations that require examination. This thesis aims to characterize the steady-state and transient heat pipe performance limitations unique to such ultra-thin form factors, and characterizes the key heat transfer mechanisms governing the performance.

A thermal resistance network model and a detailed two-dimensional model are used to analyze the steady-state performance of heat pipes under these conditions. A broad parametric study of geometries and heat inputs using the reduced-order model helps delineate the performance thresholds within which the effectiveness of a heat pipe is greater than that of a comparable solid heat spreader. A vapor-phase threshold unique to ultra-thin heat pipes operating at low power inputs is observed. At this threshold, the vapor-phase thermal resistance imposed by the saturation pressure/temperature gradient in the heat pipe causes a crossover in the thermal resistance, where performance becomes worse than a solid heat spreader. The higher-fidelity numerical model is used to assess the accuracy of the thermal resistance network model and to verify the validity and applicability of each assumption made regarding the transport mechanisms. Key heat transfer mechanisms not captured by the reduced-order thermal network models are identified. These include the effect of boundary conditions on the interface mass flux profile, convective effects on the vapor core temperature drop, and two-dimensional conduction on smearing of evaporation/condensation mass flux into the adiabatic section. Lastly, the numerical model was used to compare the transient performance between ultra-thin heat pipes and heat spreaders during the initial start-up period was conducted to demonstrate an initial crossover period under which the performance of the heat pipe was lower than that of a heat spreader.

This thesis establishes the performance thresholds of ultra-thin form factor heat pipes operating at low input heat fluxes under steady-state operation, and identifies key performance traits that must be considered under transient operation.

CHAPTER 1. INTRODUCTION

1.1 Motivation

As mobile computing devices become thinner and more powerful, efficient heat spreading technologies with matched ultra-thin form factors are called for. Heat pipes, which can have effective conductivities that are orders of magnitude larger than the intrinsic thermal conductivity of solid materials, are a viable alternative; however, demand for device thicknesses less than 1 mm imposes both practical fabrication challenges and potential performance limitations. Heat sources generating less than 1 W in these target applications are outside typical heat pipe design objectives, and recent studies have focused on increasing the maximum heat dissipation while simultaneously reducing thickness [1], as opposed to minimizing the thermal resistance at low heat fluxes. The operating conditions of ultra-thin heat pipes at low input heat fluxes brings unique performance requirements to the fore, especially in regard to user comfort that would not otherwise be central. This represents a paradigm shift in thermal management requirements, where handheld devices must maintain external surface temperatures driven by user comfort. This is often the limiting factor that determines performance throttling, rather than peak junction temperatures in the system on chip (SoC). Mobile devices also have numerous other components which may be temperature-limited (*e.g.*, the display and battery) or may dwarf the SoC heat generation under certain usage conditions (*e.g.*, the modem). This new regime of operating conditions gives rise to unique performance limitations in heat pipes.

1.2 Heat Pipe Operation

A heat pipe is a passive cooling device intended to transfer heat from a concentrated heat source either to a remote heat sink, or to spread it locally and increase the effective area available for cooling. A heat pipe consists of a porous wick structure and working fluid encapsulated in a hermetically sealed chamber usually made of a high conductivity material. Heat is transferred through phase change of the internal working fluid. The heat pipe can be considered to consist of an evaporator, condenser, and adiabatic section. The external surface of the heat pipe that is attached to the heat generating source is the evaporator; a heat pipe can have multiple heat sources attached. The surface from which heat is dissipated is called the condenser. All other surfaces are classified as the adiabatic section. When heat is added to the evaporator section, the working fluid vaporizes and the resulting increase in the vapor pressure drives the vapor flow across the adiabatic section toward the condenser section. At the condenser section, where external cooling is applied, the vapor condenses and is entrained back into the wick structure. The condensate liquid is driven back to the evaporator section due to the capillary wicking in the porous wick. The heat pipe thus transports the heat from the source to the sink using the latent heat of vaporization of the working fluid. Operation at a near-constant saturation temperature enables the heat pipe to have an effective conductivity that is many times higher than the intrinsic conductivity of pure materials.

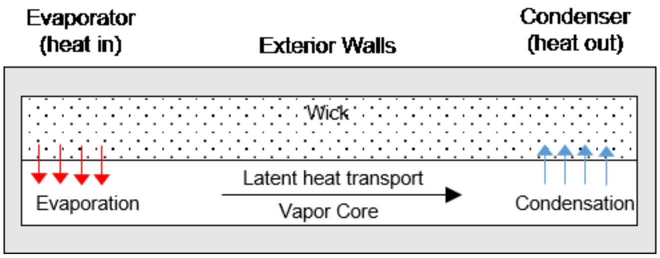

Figure 1.1. Schematic diagram of the operation of a heat pipe.

1.3 Literature Review

1.3.1 Modeling of Heat Pipe Performance

Many analytical and numerical modeling approaches have been developed to study the performance of heat pipes at varying levels of spatial and temporal fidelity, as reviewed for various types of heat pipes by Garimella and Sobhan [2] and Faghri [3]. The modeling of transport in a heat pipe is complicated due to the strong coupling between the temperature, pressure, and velocity fields in presence of liquid-vapor phase change at the interface. A simplified thermal resistance network-based analysis of heat pipe performance by Prasher [4] accurately predicted thermal resistance even under the nonuniform experimental heating conditions investigated by Chang *et al.* [5]. Vafai and Wang [6] first proposed a pseudo-three-dimensional analytical model that solved for the steady-state velocity field and axial temperature distribution assuming incompressible fluid flow; the approach was extended to include transient start-up and shutdown [7]. Aghvami and Faghri [8] developed an analytical model for prediction of the two-dimensional temperature distribution in a heat pipe and analyzed various heating and cooling configurations. Koito *et al.* [9] and Xiao and Faghri [10] developed three-dimensional, steady-state numerical models which solved for heat transport and fluid flow in the wall, vapor core, and porous wick domains.

1.3.2 Heat Pipe Transient Analysis

A two-dimensional model for the analysis of heat pipes under transient operation was developed and benchmarked against experiments by Tournier and El-Genk [11]. Vadakkan *et al.* [12, 13] developed a three-dimensional numerical model to study the transient performance of heat pipes with multiple discrete heat input sources. Ranjan *et al.* [14] coupled this device-scale numerical model with a micro-scale model that captured the vapor-liquid interface curvature effects, such as meniscus curvature and Marangoni convection, on evaporation/condensation. Carbajal *et al.* [15] analyzed the transient thermal performance of a flat heat pipe using a quasi-3D model. A transient model which coupled a 3D thermal model with a 2D hydrodynamic model was used by Sonan *et al.* [16] to investigate the performance of a flat heat pipe with multiple heat generating electronic components attached. Famouri *et al.* [17] recently performed a 2D numerical analysis of heat pipe operation implementing the transient volume-averaged gas density treatment developed by [12, 13] and proposed a selective under-relaxation method for mass transfer across the interface

1.3.3 Operating Limits of Heat Pipes

Analytical and numerical models typically do not capture other phenomena that may result in operational limits to the maximum heat transfer capacity of a heat pipe, such as entrainment of liquid into the vapor phase by shearing of the interface, local dryout at the evaporator due to boiling, and choking of the vapor flow at the sonic limit [18]. A capillary limit is commonly encountered when the pressure head provided by the wick structure at the evaporator cannot support the cumulative fluid pressure drop throughout the capillary-driven loop; vapor pressure drop is typically neglected, and the capillary limit is dictated by a working fluid figure of merit M which captures relevant liquid-phase properties. These transport-limiting phenomena prevent normal operation of the device; however, other practical design thresholds may arise when the performance of a heat pipe is unfavorable compared to a solid heat spreader under certain operating conditions and geometries. These thresholds are not fundamental limits to the maximum/minimum heat flux, but instead provide useful insight into the practicality of employing heat pipes. Sauciuc *et al.* [19] investigated the ratio of thermal resistance imposed by a flat heat pipe to that of solid copper serving as the heat spreading base of an air-cooled fin heat sink. A threshold was identified with increasing heat spreader thickness where solid copper becomes favored over the heat pipe. Device performance thresholds with decreasing thicknesses of less than 1 mm were not investigated over the range of heat input investigated (10-50 W/cm^2). Harmand *et al.* [20] presented a comparison between a heat pipe and a heat spreader for a specific geometry having multiple heat inputs. The effect of a variable heat input duty cycle on the performance of the devices was demonstrated. Owing to the complexity of solving for the complete transient solution, there is a lack of studies sufficiently covering a broad spectrum of geometric configurations and operating conditions in the literature.

1.4 Outline of Thesis

The objective of this thesis is to identify the key performance-governing transport mechanisms in ultra-thin form factor heat pipes that operate at a low input heat flux. Chapter 2 of this thesis discusses the steady-state performance of heat pipes. The heat pipe specifications and the analytical/numerical transport models are introduced. A comparison between the performance of a heat pipe and a solid heat spreader is used to identify the performance-limiting conditions. This comparison forms the basis for selecting specific test cases under which the analytical and numerical models are compared; the transport mechanisms not captured by the reduced-order model at these operating conditions are identified. A comparison between a heat pipe and solid heat spreader during the transient startup is presented in Chapter 3. Based on the steady-state analysis, a suitable geometry was chosen to explore the effects of heat input on the initial time period over which the performance of the heat pipe is worse than that of an equivalent solid heat spreader.

CHAPTER 2. PERFORMANCE-LIMITING CONDITIONS AT STEADY STATE

The important heat transfer mechanisms and practical performance thresholds that need to be taken into consideration when designing ultra-thin form factor heat pipes operating at low input heat fluxes have been identified by analyzing the steady-state performance. Using a reduced-order thermal resistance network model, a broad parametric study is conducted to assess performance as a function of geometry and heat input for a canonical heat pipe configuration. Performance is benchmarked against a solid heat spreader to define the practical performance thresholds. A subsequent comparison against the performance predicted by a higher-fidelity numerical model allows assessment of the various simplifying assumptions employed in the thermal resistance network model, thereby identifying the critical heat transfer mechanisms that may not be accounted for in a reduced-order model under these operating conditions. Material contained in this chapter was presented at the IEEE Intersociety Conference on Thermal and Thermomechanical Phenomena in Electronic Systems 2014 [21] and later submitted for journal publication [22].

2.1 Modeling Approach

The flat heat pipe configuration considered in the current study is shown in Fig. 2.1(a). The working fluid is vaporized at the wick-vapor interface as heat is applied to the evaporator section; as a result of the local pressure increase, vapor flows to the condenser end. Heat removal at the condenser causes the vapor to condense into the saturated porous wick structure, and capillary pressure pumps liquid back to the evaporator. Within the heat pipe, the wick structure lines the same side of the heat pipe as the evaporator and condenser sections to which heating and cooling boundary conditions are respectively applied. All other external walls of the heat pipe are considered to be adiabatic.

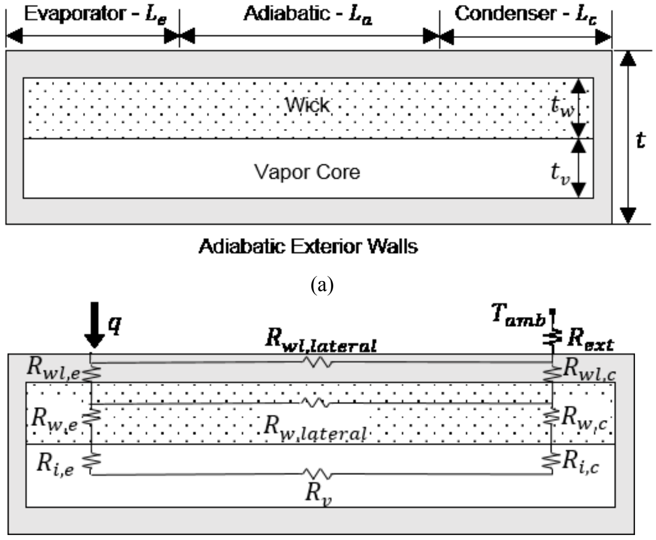

(a)

(b)

Figure 2.1. Schematic diagrams of (a) the heat pipe geometry under considerations and (b) the approximate network of thermal resistance between the evaporator and ambient.

2.1.1 Thermal Resistance Network Model

The temperature drop due to the primary heat transport mechanisms that occur in each section of the heat pipe can be represented using the simplified effective thermal resistance network shown in Fig. 2.1(b). The thermal resistances due to conduction through the thickness of the wall in the evaporator ($R_{wl,e}$) and condenser ($R_{wl,c}$) sections are negligible in the current study, which is targeted at ultra-thin heat pipes constructed from high conductivity materials. Lateral conduction along the heat pipe wall is shown as

$R_{wl,lateral}$; this thermal resistance can be calculated using an effective device length that takes into account the varying heat load along the length of the evaporator and condenser sections, given by

$$L_{eff} = L_a + \frac{L_e + L_c}{2}. \tag{1}$$

Resistances through the wick in the evaporator ($R_{w,e}$), condenser ($R_{w,c}$), and laterally across the wick ($R_{wl,lateral}$) are assumed to be due to conduction only. Convective heat transfer in the porous medium is neglected due to the small interstitial liquid velocities; hence, the liquid flow field need not be solved. An effective saturated wick thermal conductivity is used to estimate these one-dimensional conduction resistances. Lateral heat flow through the wick is neglected, owing to the high resistance that results from the low thermal conductivity and high aspect ratio wick geometry.

The interfacial phase-change thermal resistances at the wick-vapor interface in the evaporator and condenser sections, represented by $R_{i,e}$ and $R_{i,c}$, respectively, are typically small [18] and therefore neglected. The effective thermal resistance of the vapor core R_v is calculated by simplifying the vapor flow field as fully developed flow between parallel plates to estimate the pressure drop in the vapor core over the effective length. This pressure drop is related to the saturation temperature drop by applying the Clapeyron equation and ideal gas law. By this approach, an effective thermal conductivity [4] is defined for a one-dimensional lateral resistance along the effective length of the vapor

$$k_{eff,v}=\frac{h_{fg}^{2}P_{v}\rho_{v}t_{v}^{2}}{12\mathbf{R}\mu_{v}T_{v}^{2}} \tag{2}$$

where, the thermophysical properties are those of saturated vapor and are evaluated at the local vapor temperature that varies along the effective length of the device. To implement temperature-dependent vapor properties, the one-dimensional vapor thermal resistance is discretized, and each individual resistance is back-calculated from the known condenser-side temperature, and by iterating upon the heat flux passing through the vapor core. This approach does not consider convection effects within the vapor core.

Combining the system resistances yields effective heat pipe resistance

$$R_{HP}=\frac{R_{wl,lateral}(\mathrm{R}_{v}+R_{w,e}+R_{w,c})}{R_{wl,lateral}+R_{v}+R_{w,e}+R_{w,c}}. \tag{3}$$

An external heat sink resistance (R_{ext}) is included on the condenser side to replicate the realistic coupling between the ambient temperature and the heat pipe operating temperature as a function of heat load.

The model is implemented as a set of simultaneous non-linear equations in MATLAB [21], which includes temperature-dependent thermophysical vapor properties. The corresponding code is presented in Appendix B.

2.1.2 2D Numerical Model

The numerical model employed here is adapted from [12]. In summary, the model solves for the continuity, momentum, and energy equations in the wall, wick, and vapor regions of the heat pipe. Evaporation and condensation at the interface is determined from a kinetic theory-based formulation that uses the interface temperature determined from a local energy balance. To accommodate the transient changes in the mass of vapor, the vapor density is calculated from the operating pressure and local temperature using the ideal gas law; the volume-averaged liquid density is adjusted to conserve mass. All other thermophysical properties are assumed to be constant.

The liquid and vapor flow are considered to be laminar and incompressible. The continuity equation is as follows

$$\varphi \frac{\partial \rho}{\partial t} + \nabla \cdot (\rho V) = 0. \tag{4}$$

The term $\partial \rho / \partial t$ accounts for mass addition or depletion in the fluid. The momentum equations with a Brinkman-Forchheimer extended Darcy model for fluid flow in the wick region and the vapor core are

$$\frac{\partial \rho u}{\partial t} + \nabla \cdot (\rho V u) = -\frac{\partial \varphi p}{\partial x} + \nabla \cdot (\mu \nabla u) - \frac{\mu \varphi}{K} u - \frac{C_E \varphi}{\sqrt{K}} \rho |V| u \tag{5}$$

$$\frac{\partial \rho v}{\partial t} + \nabla \cdot (\rho V v) = -\frac{\partial \varphi p}{\partial y} + \nabla \cdot (\mu \nabla v) - \frac{\mu \varphi}{K} v - \frac{C_E \varphi}{\sqrt{K}} \rho |V| v \tag{6}$$

In the vapor core, permeability $K = \infty$ and porosity $\varphi = 1$. The energy equation in the wall, wick, and vapor core is

$$\frac{\partial (\rho C)_m T}{\partial t} + \nabla \cdot [(\rho C)_l V T_l] = \nabla \cdot (\mathrm{k}_{eff} \nabla T) \tag{7}$$

where, $(\rho C)_m$ assumes different values in the wall, wick, and vapor core:

$$\begin{aligned} &\text{Wall}: (\rho C)_m = (\rho C)_s \\ &\text{Wick}: (\rho C)_m = (1-\varphi)(\rho C)_s + \varphi(\rho C)_l \\ &\text{Vapor core}: (\rho C)_m = (\rho C)_v. \end{aligned} \tag{8}$$

The effective conductivity k_{eff} also assumes appropriate values in the wall, wick, and vapor core. The following boundary conditions are imposed on the domain:

1. Wick-vapor core interface: Liquid-vapor phase change is assumed to occur at the wick-vapor core interface. The interface temperature T_i is obtained from an energy balance at the interface accounting for conduction and convection on the liquid and vapor sides, and phase change

$$-k_{wick} A_i \frac{\partial T}{\partial y} + m_i C_l T_i = -k_v A_i \frac{\partial T}{\partial y} + m_i C_v T_i + m_i h_{fg} \tag{9}$$

Here $m_i < 0$ denotes evaporation and $m_i > 0$ denotes condensation. The interface pressure P_i is obtained from the Clausius-Clapeyron equation with P_0 and T_0 being reference values

$$\frac{\mathbf{R}}{h_{fg}} \ln\left(\frac{P_i}{P_0}\right) = \frac{1}{T_0} - \frac{1}{Ti} \tag{10}$$

The interface mass flux is calculated using the kinetic theory-based interfacial transport expression proposed by Schrage [22]

$$\left(\frac{2\hat{\sigma}}{2-\hat{\sigma}}\right)\left(\frac{1}{\sqrt{2\pi\mathbf{R}}}\right)\left(\frac{P_v}{\sqrt{T_v}} - \frac{P_i}{\sqrt{T_i}}\right) = m_i'' \tag{11}$$

A value of 0.03 is chosen for the accommodation coefficient $\hat{\sigma}$ as a lower bound for water [14]. The evaporated and condensed mass is assumed to flow in a direction normal to the interface when accounting for momentum transport due to phase change.

2. Wick-wall interface:

$$u = 0, v = 0 \tag{12}$$

3. Upper wall: The evaporator section has a constant heat flux condition

$$k_w \frac{\partial T}{\partial y} = q_e ; 0 \le x \le L_e \tag{13}$$

In the adiabatic section

$$\frac{\partial T}{\partial y} = 0; u = v = 0; L_e \le x \le L_e + L_a \tag{14}$$

The condenser section has a convection condition with heat transfer coefficient h_c and ambient temperature T_c

$$-k_w \frac{\partial T}{\partial y} = h_c (T - T_c);\ x > L_e + L_a \tag{15}$$

4. Lateral walls:

$$u = v = \partial T / \partial y = 0 \tag{16}$$

5. Bottom wall:

$$u = v = \partial T / \partial x = 0 \tag{17}$$

In addition the following initial conditions are imposed:

$$T(x, y, 0) = T_i ; P_{op}(t = 0) = P_{sat}(T_i) \tag{18}$$

To improve the stability of the model, and account for the coupling of interface mass flow with temperature, the mass flow rate is linearized with respect to temperature. To prevent round-off errors in the computation of pressure gradients from pressure differences that are small compared to the absolute pressure, the pressure is split into two components: a system operating pressure and a hydrodynamic component. These implementation details are discussed further in [12, 13].

The transient governing equations are discretized using the finite volume method and solved with the commercial solver FLUENT [23]. The rectangular mesh elements had a constant aspect ratio of 5 for all cases, with a size of either 0.04 mm × 0.20 mm or 0.05 mm × 0.25 mm to achieve a uniform grid over the domain for the different heat pipe geometries investigated. The wick-vapor interface conditions, evaporation and condensation mass flow rates, and fluid densities are computed with user-defined functions. In this work, steady state is considered to be achieved when the heat transfer rate in the condenser section reaches within 0.1% of the value at the evaporator section. The solution at each time step is considered converged when the residuals are less than 10^{-6} for the continuity and momentum equations, and less than 10^{-10} for the energy equation.

2.2 Results and Discussion

The thermal resistance network model allows initial performance evaluation for screening a large number of geometric permutations to identify the performance limits. Several device geometry parameters and operating conditions are fixed to specific values intended to highlight the important performance limits that occur at small device thicknesses and low input powers. For the configuration shown in Fig. 2.1(a), the length of the evaporator and condenser sections are both held constant at 10 mm, while the length of the adiabatic section and the total thickness are varied. The relative thickness of each region is fixed; the walls are 10% of the total thickness and the wick and vapor core are each 40% of the total thickness. The range of geometries investigated (10 mm < L_a < 100 mm; 0.2 mm < t < 20 mm) is intended to establish theoretical limits at extremes, and is not necessarily indicative of fabrication or material constraints. Over the range of the geometries investigated, lateral conduction resistances in the wick were found to be an order of magnitude larger than the vapor core resistance.

The heat pipe wall material is copper with a thermal conductivity of 400 W/m K. The wick consists of sintered copper powder with particle sizes in the range 45-75 μm; this particle size range allows the formation of the thin wick layers needed. The effective properties for this wick structure were characterized via x-ray microtomography-based simulations by Bodla *et al.* [24]. The wick effective thermal conductivity is 55.7 W/m K, its permeability is 1.43×10^{-11} m^2 ($C_E = 0.55$) and it supports a capillary pressure of 2250 Pa. A constant heat flux is applied to the evaporator section, and the condenser section has a convective heat transfer coefficient of 2604 W/m^2 K with an ambient temperature of 287 K.

The net resistance of the heat pipe is calculated and benchmarked against the resistance of a solid copper heat spreader with same outer dimensions. The heat spreader resistance is calculated as a one-dimensional resistance along the effective length, which accurately accounts for the effects of two-dimensional spreading near the evaporator and condenser, as confirmed by numerical simulation. When the resistance ratio R_{HP} / R_{HS} is greater than unity, the performance of the heat pipe is worse than a solid heat spreader of the same dimensions, and the condition when $R_{HP} / R_{HS} = 1$ is identified as a performance threshold. The onset of a capillary limitation is also monitored, as the heat pipe may be susceptible to this particular transport limit over the range of geometries and boundary conditions investigated. The capillary limit is enforced when

$$\Delta P_{cap,max} < \Delta P_l + \Delta P_v \tag{19}$$

where, the pressure drop in the vapor core ΔP_v is calculated assuming fully developed parallel plate flow. This physical transport limitation arrests fluid flow in the device and R_{HP} / R_{HS} is then assumed >> 1.

2.2.1 Performance Limiting Conditions

By comparing the performance across different input heat fluxes and for a range of geometries, it is possible to identify the limiting conditions that become predominant at small thickness and low input power operation. Fig. 2.2 shows a contour map of the ratio between the heat pipe and copper heat spreader thermal resistances with the adiabatic length and total thickness being varied. The dark shaded region indicates advantageous heat pipe performance, and fades to white as the ratio transitions in favor of the copper heat spreader. The performance thresholds and the capillary limit are also indicated.

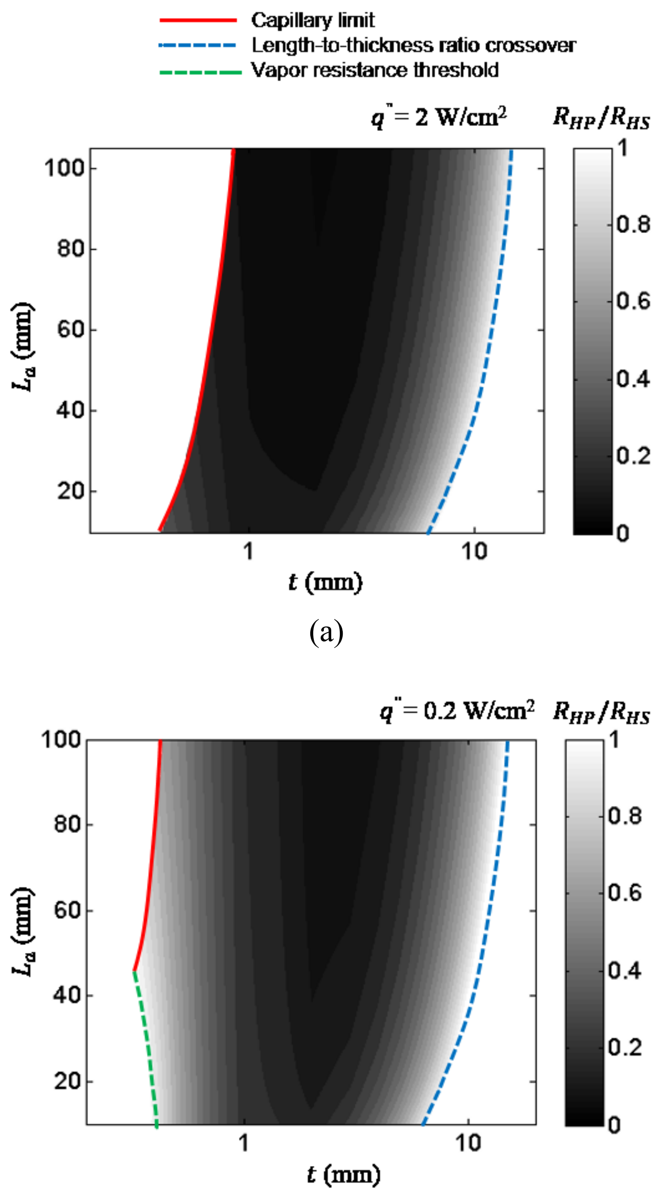

(a)

(b)

Figure 2.2. Contour map of the resistance ratio R_{HP} / R_{HS} plotted as a function of adiabatic length and thickness for an input heat flux of (a) 2 W/cm^2, and (b) 0.2 W/cm^2.

Fig. 2.2(a) shows the resistance ratio contour plot for a relatively high input heat flux of 2 W/cm^2 to illustrate the limits encountered when designing ultra-thin heat pipes for moderate power dissipation. In this case, as the thickness is reduced at a given length, the minimum thickness for which R_{HP} / R_{HS} remains greater than unity is governed by the capillary limit; a sharp transition from black to white indicates this physical transport limit. At small thicknesses and relatively high heat fluxes, the mass flow is high enough that the pressure drop along the wick and vapor core is higher than the available capillary pressure. Pressure drop in the wick is an order of magnitude larger than that across the vapor core under the conditions investigated; hence, the capillary limit-based figure of merit, M , is an appropriate design metric. In the opposite direction, with increasing device thickness, relative performance worsens for comparatively short and thick heat pipes. The performance advantage of a heat pipe comes from the small resistances incurred due to phase change and the vapor core between the evaporator and condenser ends when heat is applied to the wick structure. This advantage is lost for short, thick heat pipes, where the effective length is reduced and solid heat spreaders provide a more direct and higher-conductivity heat flow path than the heat pipe wick. This threshold at high thickness-to-length ratios has been previously acknowledged as a design guideline in the literature [19], but is not a concern for the ultra-thin devices of interest in the current study.

Fig. 2.2(b) shows the limiting conditions for the case of a much lower input heat flux of 0.2 W/cm^2. At low input heat fluxes, there is sufficient capillary pressure due to the reduced fluid velocities, and the capillary limit shifts dramatically to lower thicknesses and higher working lengths. Instead, a new threshold appears where the resistance ratio gradually favors the solid heat spreader with decreasing thickness, despite avoidance of the capillary limit. This threshold is due to the increasing pressure drop (and corresponding saturation temperature drop) along the vapor core, and therefore is identified as a vapor resistance threshold in the figure. This threshold governs the smallest device thickness at which heat pipes are beneficial, and therefore is an important limiting condition to consider for ultra-thin heat pipes operating with low heat flux input.

Despite the specific conditions for which the vapor resistance threshold is identified in Fig. 2.2(b), other important generalized conclusions may be drawn. Considering that the capillary limit is not easily reached at very low input powers, and the threshold is governed by vapor phase pressure drop, a majority of the heat pipe cross-sectional area should be reserved for the vapor core. A theoretical limit to the vapor resistance threshold can be predicted by allotting the entire cross-section to the vapor core using the analysis presented next. The validity of the analytical limit presented here hinges on the assumptions implicit in Equation (3) *viz.,* negligible transverse resistance across the wall and negligible lateral conduction across the wick. These respective assumptions are valid when $R_{wl} << (R_w + R_v / 2)$ and $R_{w,lateral} >> R_{wl,lateral} R_v / (R_{wl,lateral} + R_v)$.

It is desirable to formulate a generalized expression for the limiting thickness (on the low end) governed by the vapor resistance threshold, independent of the specific geometric constraints imposed in Fig. 2.2(b). The total thermal resistance of the heat pipe is analytically compared to the resistance of a copper heat spreader under the constraint

$$\frac{R_{HP}}{R_{HS}} < 1. \tag{20}$$

By substituting the individual thermal resistance components and representing the thicknesses of the vapor core, wick, and walls as fractions of the total thickness, i.e., $t_v = r_v t$, $t_w = r_w t$, and $t_{wl} = r_{wl} t$, the threshold conditions may be expressed as

$$\frac{r_w}{k_w}\left(\frac{1}{L_e}+\frac{1}{L_c}\right)t^4-\frac{L_{eff}}{k_s}\frac{1}{1-r_w}t^2+\frac{L_{eff}}{M_v r_v^3}=0 \tag{21}$$

Solving the equation results in two positive roots representing the thickness at both threshold conditions (vapor resistance and high thickness-to-length ratio). The limiting minimum thickness governed by the vapor resistance threshold is

$$t_{limit}=\left(\frac{\frac{L_{eff}}{k_s}a-\sqrt{\left(\frac{L_{eff}}{k_s}a\right)^2-4\frac{r_w}{k_w}\left(\frac{1}{L_e}+\frac{1}{L_c}\right)\left(\frac{L_{eff}}{M_v r_v^3}\right)}}{2\frac{r_w}{k_w}\left(\frac{1}{L_e}+\frac{1}{L_c}\right)}\right)^{\frac{1}{2}} \tag{22}$$

where, $a=1/(1-\mathrm{r}_{wl})$ and M_v is a constant representing the vapor properties. This limiting thickness is independent of the heat input (except for the influence on the vapor properties with increasing temperature for fixed condenser temperature operation); however, the capillary limit should be evaluated in conjunction with this threshold, which would be expected to prevail at any moderate heat inputs. The vapor properties dictating the vapor resistance threshold are represented as single factor that can be used as a merit number for fluid selection in the design of the ultra-thin heat pipes operating at low heat inputs

$$M_v=\frac{h_{fg}^2\rho_v P_v}{\mathbf{R}\mu_v T_v^2} \tag{23}$$

which is a combination of properties contained in the effective vapor conductivity [4], but presented in a form that excludes geometric parameters. The vapor figure of merit increases monotonically with temperature (primarily due to the strong temperature-dependence of vapor pressure and vapor density), indicative of improved performance and a reduced limiting thickness at higher temperatures. A comparison between two example working fluids, ethanol and water, to illustrate the trend in the vapor figure of merit as a function of operating temperature is presented in Appendix A.

2.2.2 Assessment of Thermal Resistance Network Model Accuracy

The above formulations hinge on the accuracy of the thermal resistance network model. The various assumptions made by the model are assessed, and provide further understanding of the prominent heat transfer mechanisms near these performance thresholds. A comparison of the heat pipe performance as predicted by the thermal resistance network model and the higher-fidelity 2D numerical model is shown in Fig 2.3. The heat pipe thicknesses investigated with the numerical model (0.4 mm, 0.5 mm, 0.6 mm, 0.8 mm, and 1 mm) are selected to span the transition toward the vapor-resistance threshold on the basis of the thermal resistance network model prediction for a device length of 40 mm. The heat pipe configuration, solid/fluid properties, geometric constraints, and boundary conditions are identical to those presented for the thermal resistance modeling results and at an input heat flux of 0.2 W/cm^2. The predictions are in reasonable agreement, with the reduced-order model predicting a lower resistance than the numerical model at small thickness and higher values at larger thickness. The differences observed at both smaller and larger thicknesses are investigated further to identify the mechanistic differences.

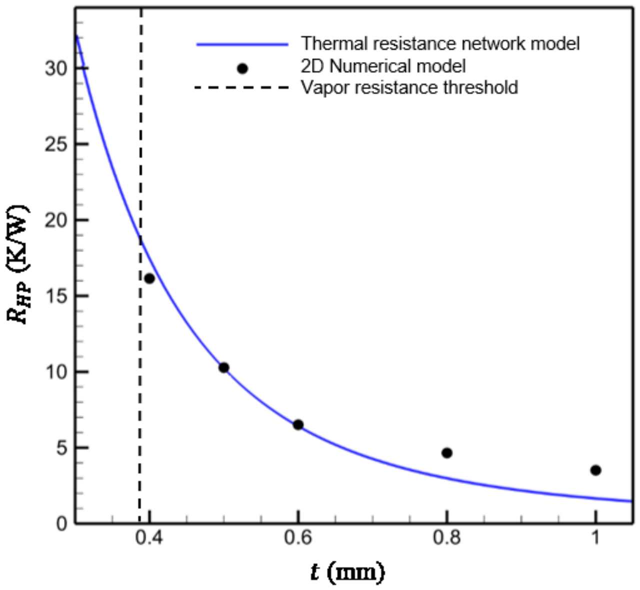

Figure 2.3. Comparison of effective thermal resistance of the heat pipe as predicted by the thermal resistance network model and 2D numerical model (L_a = 20 mm, q'' = 0.2 W/cm^2).

2.2.2.1 Heat Transfer in the Wick Region

The thermal resistance network model assumes the effective resistance of the wick in the evaporator and condenser sections is only due to conduction, and ignores advection in the porous media. To verify the validity of this assumption the temperature drop across the wick predicted by the resistance network and 2D numerical model are compared in the evaporator and condenser sections as shown in Table 2.1. There is a minor difference (< 15%) in temperature drops predicted by both models, and validates the assumption of the thermal resistance network. Further, the magnitude of the temperature drop is small and does not account for any discrepancy in the overall thermal resistance under the conditions investigated. In general, the accuracy of this assumption can be assessed by scaling the diffusive versus advective transport based on the liquid velocity in the wick structure. The Peclet number for the current cases investigated was in the order of 10^{-5}, which suggests that advection can be neglected as shown.

Table 2.1. Comparison of temperature drop across the wick in the evaporator and condenser sections

t (mm)	$\Delta T_{wick,evaporator}$		$\Delta T_{wick,condenser}$	
	2D	1D	2D	1D
0.4	0.0054	0.0050	0.0052	0.0050
0.5	0.0065	0.0065	0.0062	0.0065
0.6	0.008	0.008	0.0078	0.008
0.8	0.010	0.011	0.010	0.011
1.0	0.012	0.014	0.012	0.014

2.2.2.2 Pressure Drop across the Vapor Core

The pressure drop predicted by the thermal resistance network model assumes fully developed flow between parallel plates in the adiabatic section of the vapor core. Fig. 2.4(a) shows the gauge pressure contours and streamtraces as predicted by the numerical model ($t =$ 0.5 mm, $L_a =$ 20 mm). Fig. 2.4(b) compares the velocities at the start, center, and end of the adiabatic section to a fully developed velocity profile obtained using the pressure drop across the adiabatic section from the numerical model. Even though the maximum velocity magnitude varies slightly along the length of the adiabatic section, the fully developed flow profile is a good approximation.

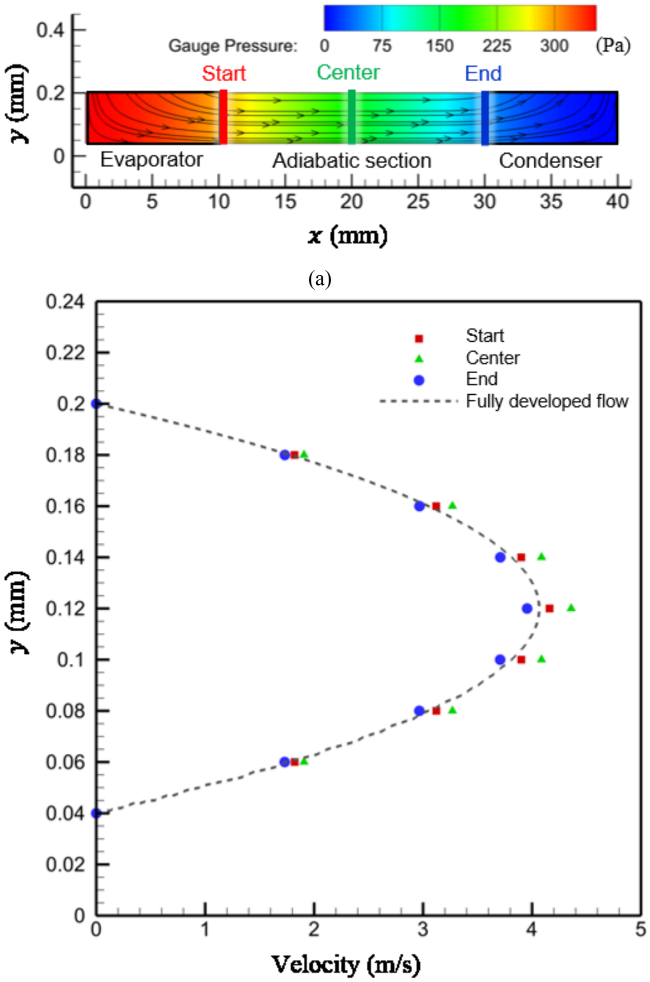

(a)

(b)

Figure 2.4. (a) Contours of gauge pressure with streamtraces overlaid in the vapor core for a heat pipe of t = 0.4 mm and L_a = 20 mm and (b) comparison of the velocities predicted by the numerical model across the adiabatic section against a fully developed velocity profile.

In the evaporator and condenser sections the flow is definitively two-dimensional. The thermal resistance network therefore assumes an effective length for which the pressure drop calculated using a fully developed flow assumption is equivalent to the actual pressure drop. The effective length used to calculate the pressure drop is based on the assumption that the rate of change of mass flux along the vapor core is constant [18].

To accurately calculate the pressure drop using this flow assumption, the mass flow rate in the vapor core calculated from the 2D numerical model has been used. A section-wise comparison of pressure drop is presented in Table 2.2. In the adiabatic section, the calculated pressure drops match as expected from interrogation of the velocity profiles in Fig. 2.4(b). Minor differences can be attributed to the imprecision in evaluation of the temperature-dependent vapor properties.

Table 2.2. Section-wise comparison of pressure drop in vapor core

t (mm)	ΔP_{evap}		ΔP_{adi}		ΔP_{cond}	
	2D	FD flow	2D	FD flow	2D	FD flow
0.4	59.0	59.1	232.9	236.0	51.8	59.1
0.5	32.7	33.2	130.6	132.8	30.2	33.2
0.6	19.7	20.1	79.6	80.3	17.7	20.1
0.8	9.4	9.8	38.2	39.0	9.0	9.8
1.0	4.9	5.1	19.9	20.4	4.7	5.1

In the sections where an effective length is used to represent the pressure drop, the accuracy of the calculations differ significantly; the calculated values match in the evaporator section and differ by as much as 14% in the condenser section. This is due to the different external boundary conditions imposed on these sections that result in different flow patterns. Fig. 2.5 shows the mass flux along the wick-vapor interface for the different thicknesses. While the constant heat flux boundary condition in the evaporator section results in an approximately flat mass flux (as assumed in the effective length used), this assumption is poor in the condenser section where the constant heat transfer coefficient boundary condition is imposed. As the thickness of the device decreases, and the interface mass flux is more closely interrelated with the external boundary conditions, and the discrepancy between the actual pressure drop and that predicted using the effective length worsens.

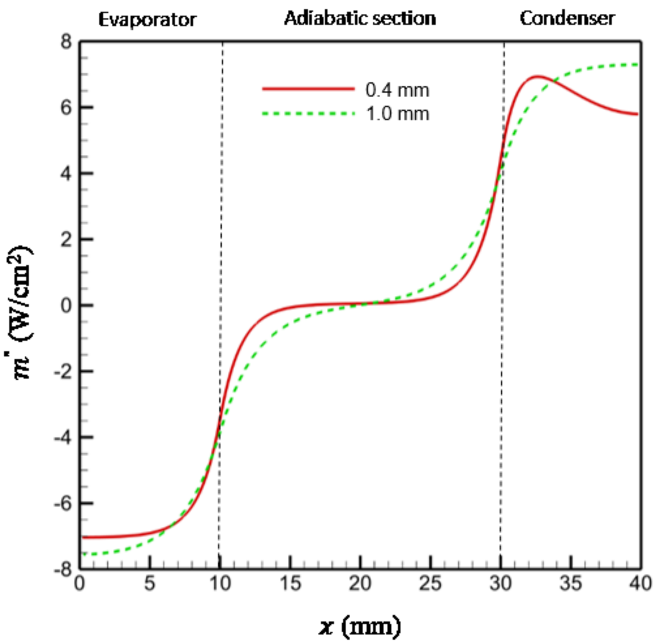

Figure 2.5. The mass flux along the wick-vapor interface for a device with $L_a = 20$ mm, and heat input $q'' = 0.2$ W/cm^2

2.2.2.3 Temperature Drop across the Vapor Core

In the thermal resistance network model, the temperature drop across the vapor core solely accounts for the change in saturation temperature as calculated using the pressure drop and Clausius-Clapeyron relation

$$\Delta T = \frac{RT^2}{p_v h_{fg}} \Delta P. \tag{24}$$

Table 2.3 shows a comparison between the temperature drop in the adiabatic section predicted using the full numerical model, and the saturation temperature change calculated using the Clausius-Clapeyron relation and pressure drop from the numerical model result. The Clausius-Clapeyron relation over-predicts the temperature drop compared to the numerical model at the smallest 0.4 mm thickness investigated due to the neglect of convective effects. This trend changes as the thickness is increased, and switches to an under-prediction.

Table 2.3. Comparison of temperature drop in the adiabatic section

t (mm)	ΔT_{adi}	
	2D	CC
0.4	1.84	2.06
0.5	1.06	1.14
0.6	0.68	0.72
0.8	0.38	0.33
1.0	0.26	0.17

To understand the reason for the under-prediction of temperature drop at larger thicknesses, Fig. 2.6 shows a comparison of the temperature variations along the centerline of the adiabatic section between the numerical model and the Clausius-Clapeyron relation. The temperature gradients are in fair agreement at the center of the adiabatic section where there is not any mass flux into or out of the vapor core (Fig. 2.5). While the temperature gradient is in agreement at the center of the adiabatic section, there is significant deviation at either ends of the section. This disagreement can be explained by observing the spreading of heat, and thereby mass flux, into the vapor core that occurs at larger thicknesses, as can be observed in Fig. 2.5. As parts of the adiabatic section contribute to evaporation and condensation at either ends, the temperature drop calculated by implementing the Clausius-Clapeyron relation, which does not account for the addition of mass flux into the control volume when relating the temperature drop with pressure drop, is no longer accurate.

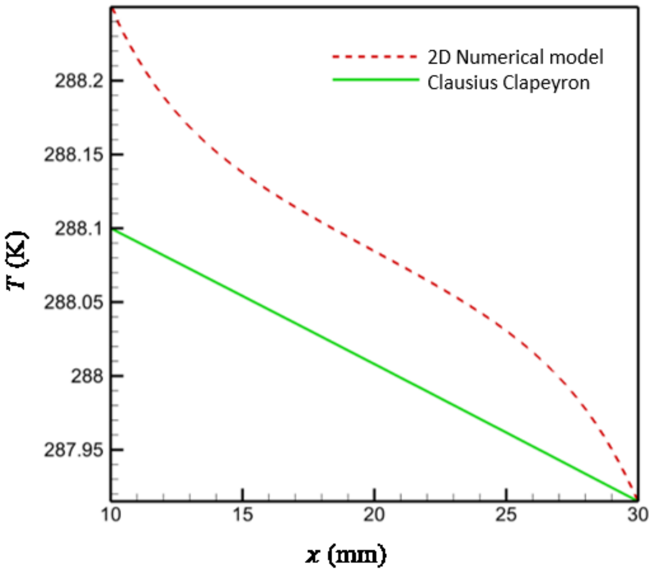

Figure 2.6. Temperature variation along the centerline of the adiabatic section for a heat pipe with $t =$ 1.0 mm and $L_a =$ 20 mm.

The thermal resistance network model is remarkably accurate over the range of device thicknesses investigated considering the numerous simplifying assumptions employed; however, the comparison between the 2D numerical model and the thermal resistance network model reveals several drawbacks of such simplifications. The mass flux profile at the wick-vapor interface is significantly influenced by the boundary conditions in the evaporator and condenser sections, which invalidates the conventional effective length used for pressure drop calculations. Convective effects in the vapor core reduce the temperature drop at very small thicknesses, and spreading of the evaporation/condensation mass flux into the adiabatic section increases the temperature drop at larger thicknesses.

CHAPTER 3. EXPLORATORY ANALYSIS OF TRANSIENT PERFORMANCE THRESHOLDS

3.1 Introduction

In the previous chapter, a comparison between the steady-state performance of a heat pipe and solid heat spreader was presented. The thermal resistance network model was used to generate performance contours which suggested a region of interest where the heat pipe performance is superior. However, the thermal resistance network model does not give any information on the temporal performance domain during the initial startup time before the device reaches steady state (or when the device may be subjected to a varying heat input) that occurs during realistic operation. This evaluation of the transient performance is of extreme importance in mobile applications because of the various heat-generating components that are intermittently used during typical operation of the device. There has been no previous investigation that aims to map out the temporal resistance ratio, R_{HP} / R_{HS} , as was done for steady-state operation in Chapter 2. This chapter probes such performance characteristics during transient operation. A comparison between the thermal resistance of heat pipe and solid copper heat spreader during initial startup is presented for a selected geometry and operating condition. Based on the transient response of the heat pipe, an example case study of a transient heat input is also investigated.

The numerical model as described in Section 2.1.2 is a fully transient modeling approach that allows for analysis of the transient performance characteristics. The computational cost required to solve for the transient characteristics precludes an extensive parametric study of many geometries and heat inputs, as was done using the thermal resistance network model for steady-state analysis. Instead, transient start-up test cases have been chosen based on the various performance-limiting conditions observed at steady state. Based on the steady-state performance contours presented in Fig. 2.2, the transient test cases are chosen such that they fall within the region where heat pipes outperform solid spreaders. The possibility for dry-out due to a capillary limit was avoided during selection of the test cases.

3.2 Results and Discussion

The test case geometry chosen has a device length of 40 mm and thickness of 0.8 mm. The other geometric parameters, such as the thickness of the wall, wick, and vapor core, are kept identical to those described in Chapter 2; *i.e.,* the outer walls are 10% of the total thickness (0.08 mm) on either side; and the wick and vapor core are 40% of the total thickness (0.32 mm). The performance is compared to a copper heat spreader of the same external dimensions. Both devices are at an initial temperature of 287 K before the heat input is applied. Fig. 3.1(a) shows comparison between the path to steady state for a heat pipe and solid heat spreader under the application of a constant heat input of $q'' =$ 0.2 W/cm^2. Fig. 3.1(b) shows the comparison over a much shorter initial time. The steady-state temperature drop across the heat pipe is smaller than that of the solid heat spreader (as expected based on the thermal resistance modeling predictions); the heat pipe also reaches steady state faster than the solid heat spreader. However, Fig. 3.1(b) reveals a very brief time period, on the order of seconds, over which the heat pipe performance is actually lower than the solid heat spreader. The time at which the performance of the heat pipe and solid heat spreader are equivalent is identified as the crossover time (1.1 s for the selected case). This initial period of inferior heat pipe performance can be attributed to the time it takes for the working fluid to vaporize and build up sufficient vapor pressure to drive flow across the vapor core. Further understanding of this mechanism, and generalized mapping of the crossover time, may be very important to applications that intend to utilize ultra-thin heat pipes for thermal management in transient scenarios. Specifically, this behavior may determine overheating/failure during the initial startup, and is also useful for anticipating the transient performance under the application of a varying input heat.

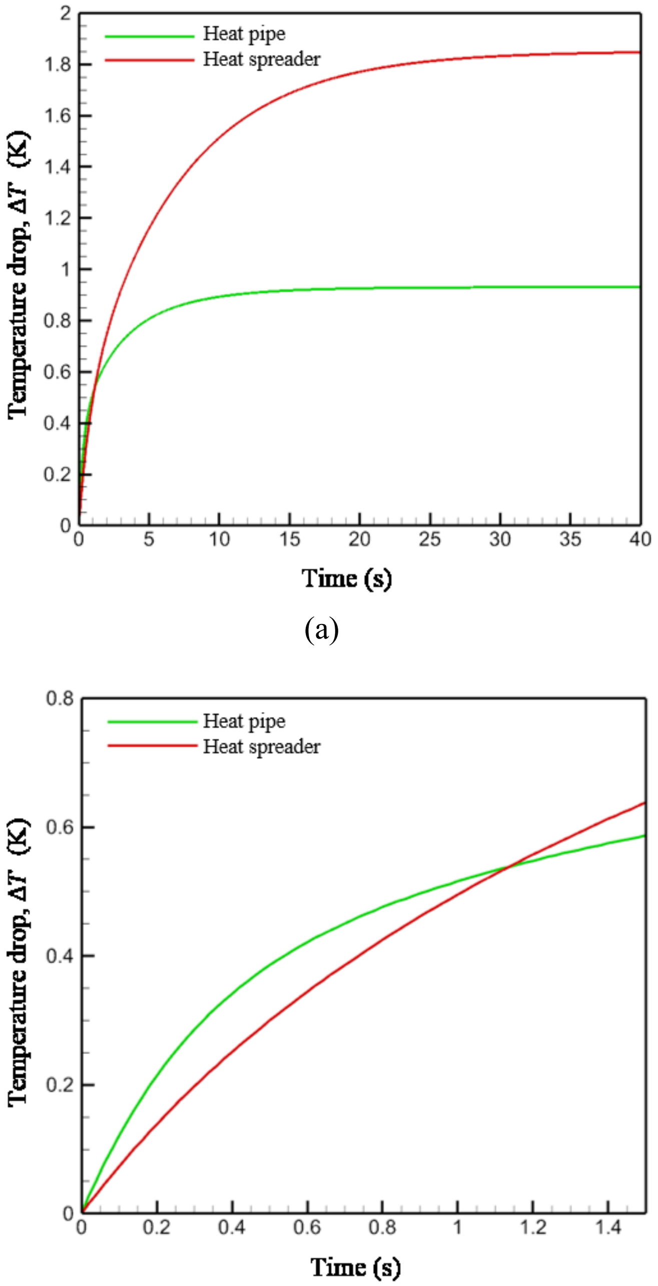

(a)

(b)

Figure 3.1. (a) Comparison of the path to steady state between a heat pipe and a solid heat spreader for a heat input of $q'' = 0.2$ W/cm^2; (b) a zoomed in view of the comparison over the first 1.5 s of heat pipe operation is also shown.

A preliminary analysis of variations in the path to steady state for different heat inputs is conducted for the selected heat pipe geometry. The different heat inputs are compared in Fig 3.2, using a normalized temperature drop for each case studied defined as

$$\Delta T_{normalized} = \frac{\Delta T}{\Delta T_{steady\ state}}. \tag{25}$$

As the input heat increases, the heat pipe device reaches steady state faster. The larger heat input vaporizes the working fluid and causes the vapor pressure to build up faster, expediting the time to steady state.

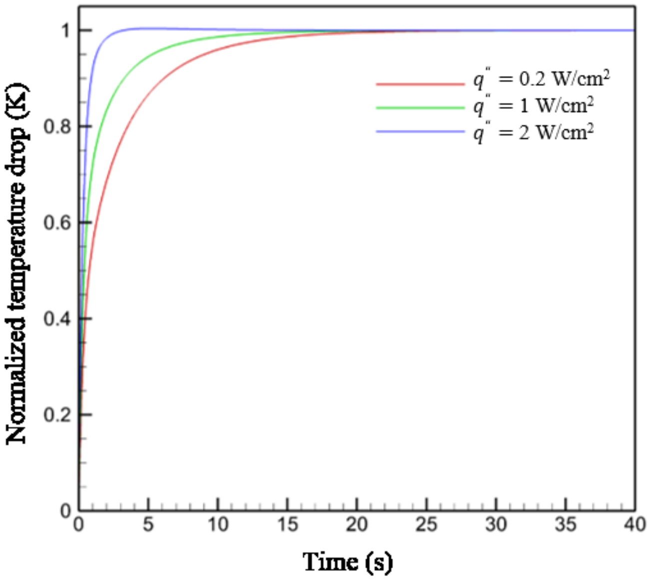

Figure 3.2. Comparison of normalized temperature drop across a heat pipe with $L_a = 20\ mm$ and $t = 0.8\ mm$ for various input heat fluxes.

The existence of a crossover time and differences in the transient path between the heat pipe and solid heat spreader complicate the choice of device to be employed for transient heat input duty cycles. As example, a transient heat input case is explored where there is a 1 s pulse of constant input heat flux at 2 W/cm^2. A comparison of the evaporator temperature rise, between a heat pipe and solid heat spreader, is presented in Fig 3.3. Within the initial pulse, the performance crossover time is reached during startup, and the heat pipe is at a lower temperature at the end of the pulse. Once the heat input ceases, the heat pipe temperature falls faster, resulting in an extended period of superior performance compared to the solid heat spreader. This example case highlights the importance of analyzing the various actual transient input heat cycles a device may be subjected to in the field; these transients may in fact determine the performance limits and geometric design of the device.

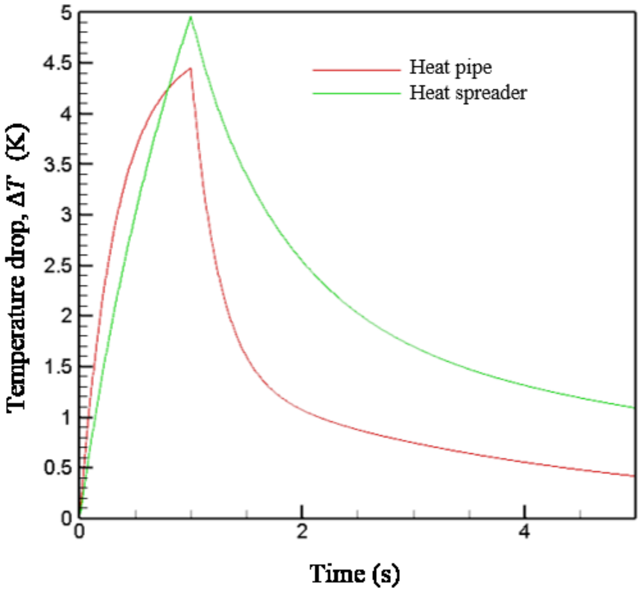

Figure 3.3. Comparison of the temperature drop between a heat pipe and a solid heat spreader for a 1 s pulse of 2 W/cm^2 input heat flux for a device of $L_a = 20\,mm$ and $t = 0.8\,mm$.

The analysis presented in this chapter provides a preliminary understanding of ultra-thin heat pipe performance during the initial transient startup period. Using example geometries and boundary conditions to compare against a solid heat spreader, the existence of a crossover time was demonstrated. Variations in heat pipe response times as a function of the heat input were also presented. An example transient input heat case showed the importance of considering operational transients when determining the performance limitations of ultra-thin heat pipes.

CHAPTER 4. CONCLUSIONS

4.1 Summary and Conclusions

The performance of ultra-thin form factor heat pipes was simulated using a thermal resistance network model and a higher-fidelity numerical model. Using the thermal resistance network model, it was shown that the limiting smallest heat pipe thickness is defined by a vapor resistance threshold at low input heat fluxes. At this threshold, pressure drop in the vapor core causes a higher effective thermal resistance compared to a solid heat spreader. An analytical evaluation of this threshold revealed a relationship between the limiting thickness and the governing vapor properties, which is captured by defining a vapor-phase figure of merit as a criterion for working fluid selection. A detailed comparison between the numerical model and the thermal resistance network model was presented, and each of the simplifying assumptions made by the reduced-order model analyzed. The thermal resistance network, though remarkably accurate given its simplicity, fails to capture several key heat transfer mechanisms that may affect the performance of ultra-thin heat pipes. These include the effects of external boundary conditions on the interfacial mass flux profile, convection in the vapor core, and smearing of the interfacial mass flux into the adiabatic section by two-dimensional conduction. The thermal resistance network model is able to capture the transport mechanisms that govern heat pipe overall thermal resistance, and may be relied upon to develop approximate design guidelines; however, these additional mechanisms should be accounted for in detailed numerical models for application-oriented design and optimization of ultra-thin form factor heat pipes. A preliminary analysis of the performance characteristics during transient operation was presented. Using a selected geometry, the effect of heat input on the time taken to reach steady-state was probed, and the temporal performance compared to that of a solid heat spreader. An example transient heat input cycle was also demonstrated.

4.2 Recommendations for Future Work

The work in this thesis represented a broad overview of the various limitations encountered in designing for such ultra-thin form factors; however, several additional studies should be considered to build upon this framework:

- A better generalized and predictive understanding of the various limitations presented, which were specific to the operating conditions investigated, needs to be developed.
- A more extensive study of the transient performance-limiting conditions should be conducted, so as to fully map the temporal performance compared to solid heat spreaders (as was done for the steady-state performance in this thesis); transient analysis was limited to selected cases in the current study on account of the modeling expense, and would require further development and use of reduced-order transient models appropriate for ultra-thin form factor devices.
- The current study used a selected wick structure; a detailed study of the effects of wick microstructure on the performance limitations could be investigated; further,

given the larger number of geometric parameters and possible permutations of the various components, heat pipes provide a rich optimization problem that may enable widening of the performance envelope.

LIST OF REFERENCES

LIST OF REFERENCES

[1] J. A. Weibel and S. V. Garimella, "Recent Advances in Vapor Chamber Transport Characterization for High-Heat-Flux Applications," *Advances in Heat Transfer,* vol. 45, pp. 209-301, 2013.

[2] S. V. Garimella and C. B. Sobhan, "Recent Advances in the Modeling and Applications of Nonconventional Heat Pipes," *Advances in Heat Transfer,* vol. 35, pp. 249-308, 2001.

[3] A. Faghri, "Review and Advances in Heat Pipe Science and Technology," *Journal of Heat Transfer,* vol. 134, p. 123001, 2012.

[4] R. S. Prasher, "A Simplifed Conduction Based Modeling Scheme for Design Sensitivity of Thermal Solution Utilizing Heat Pipe and Vapor Chamber Technology," *Journal of Electronic Packaging,* vol. 125, pp. 378-385, 2003.

[5] J. Y. Chang, R. S. Prasher, S. Prstic, P. Cheng and H. B. Ma, "Evaporative Thermal Performance of Vapor Chambers Under Nonuniform Heating Conditions," *Journal of Heat Transfer,* vol. 130, p. 121501, 2008.

[6] K. Vafai and W. Wang, "Analysis of Flow and Heat Transfer Characteristics of an Asymmetrical Flat Plate Heat Pipe," *International Journal of Heat and Mass Transfer,* vol. 35, pp. 2087-2099, 1992.

[7] Y. Wang and K. Vafai, "Transient Characterization of Flat Plate Heat Pipes During Startup and Shutdown Operations," *International Journal of Heat and Mass Transfer,* vol. 43, pp. 2641-2655, 2000.

[8] M. Aghvami and A. Faghri, "Analysis of Flat Heat Pipes with Various Heating and Cooling Configurations," *Applied Thermal Engineering,* vol. 31, pp. 2645-2655, 2011.

[9] Y. Koito, H. Imura, M. Mochizuki, Y. Saito and S. Torii, "Numerical Analysis and Experimental Verification on Thermal Fluid Phenomena in a Vapor Chamber," *Applied Thermal Engineering,* vol. 26, pp. 1669-1676, 2006.

[10] B. Xiao and A. Faghri, "A Three-Dimensional Thermal-Fluid Analysis of Flat Heat Pipes," *International Journal of Heat and Mass Transfer,* vol. 51, pp. 3113-3126, 2008.

[11] J. M. Tournier and M. S. El-Genk, "A Heat Pipe Transient Analysis Model," *Internantional Journal of Heat and Mass Transfer,* vol. 37, pp. 753-762, 1994.

[12] U. Vadakkan, J. Y. Murthy and S. V. Garimella, "Transient Analysis of Flat Heat Pipes," in *Proceedings of the ASME Summer Heat Transfer Conference (SHTC)*, Las Vegas, NV, USA, July 21–23, 2003.

[13] U. Vadakkan, S. Garimella and J. Murthy, "Transport in Flat Heat Pipes at High Heat Fluxes from Multiple Discrete Sources," *Journal of Heat Transfer,* vol. 126, pp. 347-354, 2004.

[14] R. Ranjan, J. Murthy, S. Garimella and U. Vadakkan, "A Numerical Model for Transport in Flat Heat Pipes Considering Wick Microstructure Effects," *International Journal of Heat and Mass Transfer,* vol. 54, pp. 153-168, 2011.

[15] G. Carbajal, C. Sobhan, G. ‘. Peterson, D. Queheillalt and H. N. Wadley, "A Quasi-3D Analysis of the Thermal Performance of a Flat Heat Pipe," *International Journal of Heat and Mass Transfer,* vol. 50, pp. 4286-4296, 2007.

[16] R. Sonan, S. Harmand, J. Pellé, D. Leger and M. Fakès, "Transient Thermal and Hydrodynamic Model of Flat Heat Pipe for the Cooling of Electronics Components," *International Journal of Heat and Mass Transfer,* vol. 51, pp. 6006-6017, 2008.

[17] M. Famouri, G. Carbajal and C. Li, "Transient Analysis of Heat Transfer and Fluid Flow in a Polymer-Based Micro Flat Heat Pipe with Hybrid Wicks," *International Journal of Heat and Mass Transfer,* vol. 70, pp. 545-555, 2014.

[18] D. Reay and P. Kew, Heat Pipes: Theory, Design, and Applications, 5th ed., Butterworth-Heinemann, 2006.

[19] I. Sauciuc, G. Chrysler, R. Mahajan and R. Prasher, "Spreading in the Heat Sink Base: Phase Change Systems or Solid Metals??," *IEEE Transactions on Components and Packaging Technologies,* vol. 25, pp. 621-628, 2002.

[20] S. Harmand, R. Sonan, M. Fakès and H. Hassan, "Transient cooling of electronic components by flat heat pipes," *Applied Thermal Engineering,* vol. 31, pp. 1877-1885, 2011.

[21] Y. Yadavalli, J. A. Weibel and S. V. Garimella, "Flat Heat Pipe Performance Thresholds at Ultra-Thin Form Factors," in *IEEE Intersociety Conference on Thermal and Thermomechanical Phenomena in Electronic Systems (ITHERM)*, Orlando, FL, USA, May 27-30, 2014.

[22] Y. Yadavalli, J. A. Weibel and S. V. Garimella, "Performance-Governing Transport Mechanisms for Heat Pipes at Ultra-Thin Form Factors," *(in review),* 2014.

[23] The MathWorks Inc., "MATLAB," 2011.

[24] R. Schrage, A Theoretical Study of Interface Mass Transfer, New York: Columbia University Press, 1953.

[25] ANSYS Inc., ANSYS FLUENT User's Guide, Release 14.0 ed., 2011.

[26] K. Bodla, J. Murthy and S. Garimella, "Direct Simulation of Thermal Transport Through Sintered Wick Microstructures," *Journal of Heat Transfer,* vol. 134, p. 012602, 2011.

APPENDICES

Appendix A Comparison of Ethanol and Water as Working fluids

A comparison between two example working fluids, ethanol and water, to illustrate the trend in the vapor figure of merit as a function of operating temperature (left axis) and the limiting thickness based on the vapor resistance threshold (right axis) is presented in Fig.A.1. The vapor figure of merit increases monotonically with temperature (primarily due to the strong temperature-dependence of vapor pressure and vapor density), indicative of improved performance and a reduced limiting thickness at higher temperatures. The magnitude of the limiting thickness also indicates that the vapor resistance threshold only has practical implications (t_{limit} > 0.1 mm) at temperatures less than approximately 47 °C; however, this is a reasonable range for mobile computing devices with external skin temperatures ergonomically limited to less than 44 °C. Also of note are the superior characteristics of ethanol compared to water based on the vapor figure of merit, M_v, over the entire temperature range. This is in contrast to the commonly referenced capillary limit-based figure of merit, M, which would suggest water as the better working fluid in this temperature range. This conventional view of water as the ideal heat pipe working fluid for operational temperatures associated with electronics cooling applications therefore does not necessarily apply to ultra-thin heat pipes with low input heat fluxes.

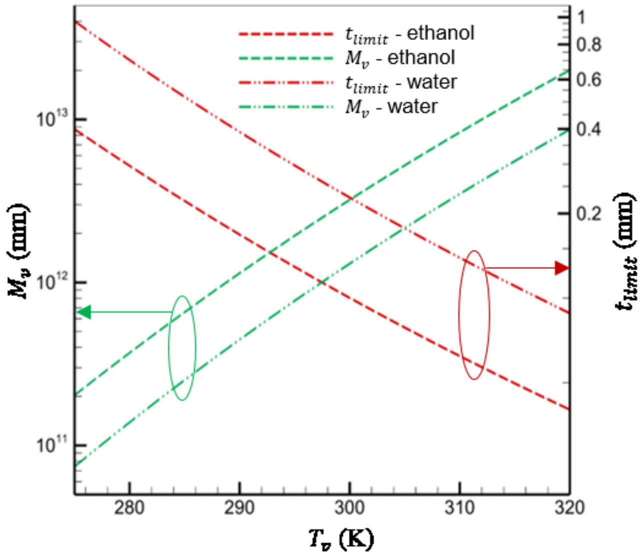

Figure A 1. Vapor figure of merit (left axis) and corresponding limiting thickness for the present heat pipe configuration shown in Fig. 2.1(a) (r_w = 0.4, r_v = 0.4, and r_{wl} = 0.1; L_a = 20mm) (right axis) as a function of temperature for ethanol and water.

The numerical model is used to support the conclusions derived from the thermal resistance network model. Fig.A.2 shows a comparison of the temperature contours using ethanol versus water as the working fluid in an ultra-thin heat pipe device (t = 0.5 mm and L_a = 20 mm) at an input heat flux of 0.2 W/cm^2. The observation of improved performance for ethanol is in agreement with the thermal resistance network model; the effective thermal resistance using ethanol and water are calculated to be 4.18 and 9.60 m^{2}K/W, respectively.

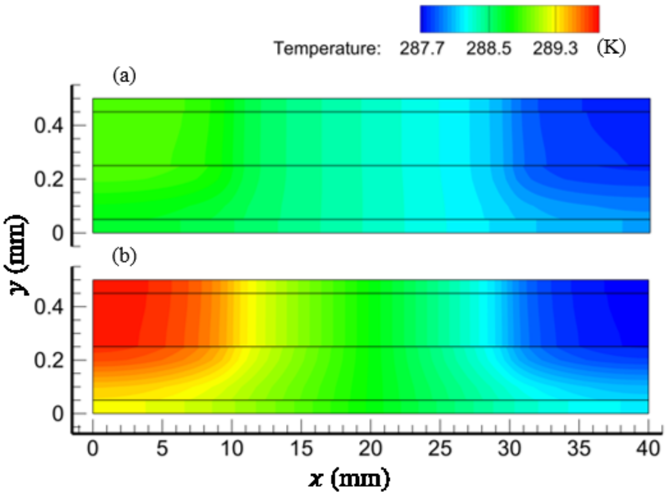

Figure A 2. Temperature contours for a heat pipe ($t =$ 0.5 mm and $L_a =$ 20 mm) with (a) ethanol and (b) water as the working fluid.

Appendix B MATLAB Code for Solving the Thermal Resistance Network

```
% Heat pipe effective resistance for a single device
clear all

% Wick Thermophysical Properties 45-75 micron
K = 2.51e-11; % Permeability
dP_max = 2250; % Max capillary pressure
k.eff = 55.66; % Effective thermal conductivity of wick
k.cu = 387.6; % Thermal conductivity of copper

% Heat Pipe Dimensions
w = 10e-3; % Width
L.e = 10e-3; % Evaporator length
L.c = 10e-3; % Condenser length
L.a = 20e-3; % Adiabatic length
L.eff = L.a + 0.5*(L.e+L.c); % Effective length

t = 0.8*1e-3; % Total thickness
vap.t = 0.4*t; % Vapor core thickness
wick.t = 0.4*t; % Wick thickness
wall.t = 0.1*t; % Wall thickness

% External conditions
Q = 5; % Input Heat Flux
h = 2604; % Heat transfer coefficient
R_ext = 1/(h*L.c*w); % External resistance
T.amb = 287; % Ambinet Temperature
T.cond = Q*R_ext + T.amb; % Condenser Temperature

% Wick and wall resistances
wick.R = wick.t/(k.eff*L.e*w); % Wick Thermal Resistance
wick.Rlat = L.a/(k.eff*wick.t*w); % Wick Lateral Resistance
wall.Rlat = L.a/(k.cu*wall.t*w); % Wall Lateral Resistance

% Vapor resistance
h_fg = 2473000; % Latent heat
u_v = 9.5e-06; % Vapor viscosity
R = 461.5; % Gas constant

% Discretize the effective length into N cells
N = 120;
dx = L.eff/N;
Tv = zeros(N+1,1);
kv = zeros(N,1);
Rv = zeros(N,1);
dPv = zeros(N,1);
Pv = zeros(N,1);
```

```matlab
Tv(1) = T.cond + (0.75*Q)*wick.R;
Pv(1) = refpropm('P','T',Tv(1),'Q',1,'water')*1000;
vap.qnew = Q;
vap.qold = 0;
iter = 0;
while abs(vap.qold-vap.qnew)>10e-06
    iter = iter+1;
    for i = 1:N
        % Thermophysical properties
        rho_v = refpropm('D','T',Tv(i),'Q',1,'water'); % Vapor density
        p_v = refpropm('P','T',Tv(i),'Q',1,'water')*1000; % Vapor pressure
        kv(i) = (h_fg^2*p_v*rho_v*vap.t^2)/(12*R*u_v*Tv(i)^2); % Conductivity
        Rv(i) = dx/(kv(i)*vap.t*w); % Vapor Core Thermal Resistance

        dPv(i) = 12*u_v*vap.qnew/h_fg/rho_v*(dx/vap.t^3/w); % Vapor pressure drop
        Tv(i+1) = Tv(i) + vap.qnew*Rv(i);
        Pv(i+1) = Pv(i) + dPv(i);
    end
    vap.R = sum(Rv); % Net vapor resistance
    vap.dP = sum(dPv); % Net vapor pressure drop

    % Liquid thermophysical properties
    liq.u = refpropm('V','T',T.cond,'Q',0,'water'); % Viscosity of water
    liq.rho = refpropm('D','T',T.cond,'Q',0,'water'); % Density of water
    liq.dP = liq.u*L.eff*Q/h_fg/liq.rho/K/wick.t/w; % Liquid pressure drop

    % Resistance ratios
    R_HS = L.eff/(k.cu*t*w); % Heat spreader resistance
    % Heat pipe resistance
    R_HP2 = vap.R + 2*wick.R;
    R_HP = (R_HP2*wall.Rlat)/(R_HP2+wall.Rlat);
    T.evap = Q*R_HP + T.cond;
    ratio.R = R_HP/R_HS; %Resistance ratio
    ratio.P = (vap.dP + vap.dP)/dP_max; %Pressure ratio

    % Heat fluxes
    wall.q = (T.evap-T.cond)/wall.Rlat;
    vap.q = (T.evap-T.cond)/R_HP2;

    % Temperature drops
    wick.dT = wick.R*vap.q;
    vap.dT = vap.R*vap.q;

    % update predictions
    vap.qold = vap.qnew;
    vap.qnew = vap.q;
end
```

PUBLICATIONS

PUBLICATIONS

Y. Yadavalli, J. A. Weibel and S. V. Garimella, "Performance-Governing Transport Mechanisms for Heat Pipes at Ultra-Thin Form Factors," *(in review),* 2014.

Y. Yadavalli, J. A. Weibel and S. V. Garimella, "Flat Heat Pipe Performance Thresholds at Ultra-Thin Form Factors," in *IEEE Intersociety Conference on Thermal and Thermomechanical Phenomena in Electronic Systems (ITHERM)*, Orlando, FL, USA, May 27-30, 2014.